IOP Publishing Phys. Med. Biol. 65 (2020) 065006 https://doi.org/10.1088/1361-6560/ab7502

Physics in Medicine & Biology

IPEM Institute of Physics and Engineering in Medicine

PAPER

RECEIVED
24 November 2019

ACCEPTED FOR PUBLICATION
11 February 2020

PUBLISHED
20 March 2020

Cerenkov luminescence and PET imaging of ^{90}Y: capabilities and limitations in small animal applications

Gregory S Mitchell, P N Thomas Lloyd and Simon R Cherry

Department of Biomedical Engineering, University of California, Davis, One Shields Avenue, Davis, CA 95616, United States of America

E-mail: gsmitchell@ucdavis.edu

Keywords: Cerenkov radiation, Cerenkov luminescence, optical imaging, yttrium-90 imaging

Abstract

The *in vivo* sensitivity limits and quantification performance of Cerenkov luminescence imaging have been studied using a tissue-like mouse phantom and ^{90}Y. For a small, 9 mm deep target in the phantom, with no background activity present, the Cerenkov luminescence ^{90}Y detection limit determined from contrast-to-noise ratios is 10 nCi for a 2 min exposure with a sensitive CCD camera and no filters. For quantitative performance, the values extracted from regions of interest on the images are linear within 5% of a straight line fit versus target activity for target activity of 70 nCi and above. The small branching ratio to decay with positron emission for ^{90}Y also permits low-statistics PET imaging of the radionuclide. For PET imaging of the same phantom, with a small animal LSO detector-based scanner, the ^{90}Y detection limit is approximately 3 orders of magnitude higher at 10 μCi.

1. Introduction

Cerenkov luminescence imaging (CLI) is a promising option for molecular imaging in small animals (Ruggiero *et al* 2010, Mitchell *et al* 2011, Robertson *et al* 2011, Xu *et al* 2012, Ciarrocchi and Belcari 2017) or in clinical intraoperative applications (Liu *et al* 2012, Chi *et al* 2014, van Leeuwen *et al* 2015, Hu *et al* 2015, Grootendorst *et al* 2016). In some uses it can combine the strengths of nuclear medicine (small molecule radiotracers; clinically approved probes; facile radiochemistry labeling) with the strengths of optical imaging (rapid image acquisition and high throughput; relatively inexpensive imaging systems).

The goal of this study was to use a mouse phantom with tissue-like optical properties to explore the limits of *in vivo* sensitivity and quantification performance of preclinical CLI with ^{90}Y. Additionally a comparison was made to the use of PET to image ^{90}Y.

^{90}Y is a radionuclide seeing growing clinical use. It has a 64-h half-life making it useful for radioimmunotherapy (Larson *et al* 2015) or radioembolization (Pasciak *et al* 2014) procedures. Chelation (Kukis *et al* 1998, De León-Rodríguez and Kovacs 2008) allows straightforward labeling of many biological molecules with Y. ^{90}Y decays almost exclusively by emission of a beta-minus (β^-), with energy of up to 2.28 MeV, making it especially useful for radiotherapy applications. In order to determine the biodistribution of ^{90}Y, SPECT imaging using the emitted bremsstrahlung x-rays (emitted as the β^-slows down in tissue) has been used with some success (Minarik *et al* 2008, Wright *et al* 2015). Interestingly, ^{90}Y has a small (32×10^{-6}) branching ratio to decays which emit a positron (Nickles *et al* 2004, Selwyn *et al* 2007, D'Arienzo 2013). This arises from rare decays to the 1.76 MeV 0+ ^{90}Zr state which then undergoes an electric monopole transition to the ground state; in doing so it decays by internal conversion, emission of two gamma rays, or by pair production (i.e. emission of a β^- and β^+). The presence of the β^+ enables PET imaging, and increasingly for ^{90}Y imaging PET is being used clinically in preference to bremsstrahlung SPECT (Barber *et al* 2013, Elschot *et al* 2013, Padia *et al* 2013, Attarwala *et al* 2014, Pasciak *et al* 2014, Takahashi *et al* 2015), as the SPECT images obtained are typically of fairly poor quality due to low statistics and the low energy of the photons. PET imaging of ^{90}Y has been studied in multicenter phantom trials (Willowson *et al* 2015, Maughan *et al* 2018) and as imaging experience grows, acquisition and reconstruction parameters can be optimized (Scott and McGowan 2019). One other option for PET imaging of Y to note is

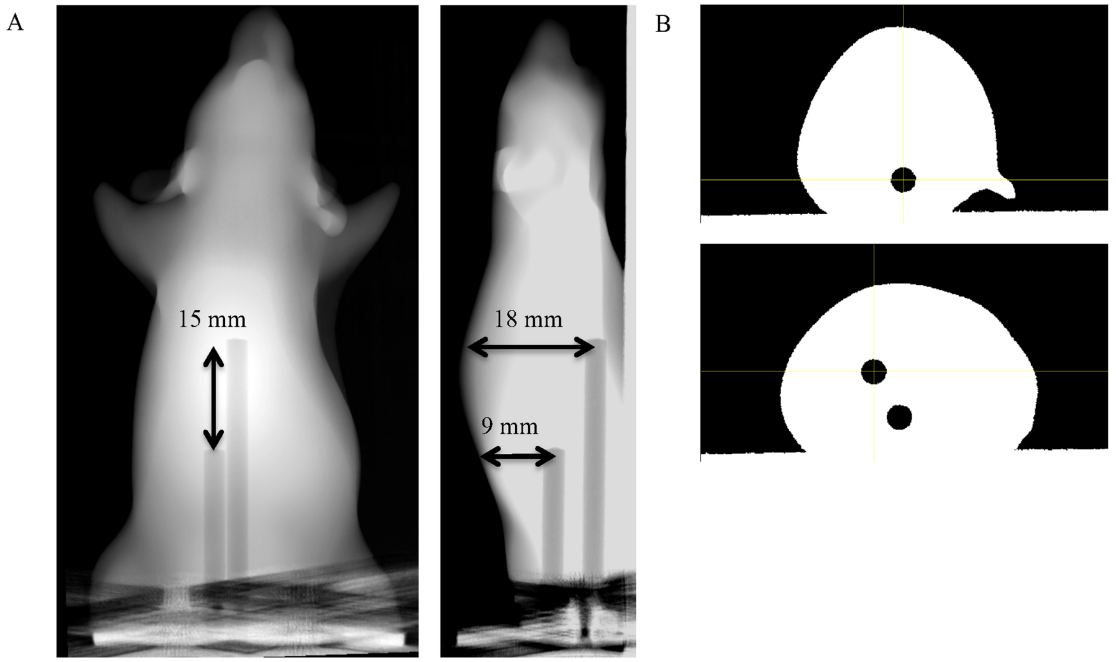

Figure 1. Mouse phantom CT scan projections (A) and thresholded slices (B) showing the location of the two insert openings. Viewed from the dorsal side, the end of the left insert is 9 mm vertically below the phantom surface and the other insert end is 18 mm deep. The axial locations of the ends of the holes are 15 mm apart. From the ventral side the target locations are 10 mm from the surface and 4 mm for the central location. At the tail end of the phantom the CT scan shows artifacts from two metal screws.

the isotope ^{86}Y (Nayak and Brechbiel 2011), which has a 14-h half life and is a positron emitter (32%), but ^{86}Y also emits many other prompt gamma rays (on average 3 per decay) making PET imaging challenging (Lubberink and Herzog 2011). While some progress has been made on ^{86}Y production (Yoo *et al* 2005), its cost and availability are at the moment not favorable compared to ^{90}Y.

In addition to PET imaging, optical imaging is possible for ^{90}Y. Due to the relatively high β-decay energy, ^{90}Y is one of the brightest medical radionuclide emitters of Cerenkov radiation, emitting approximately 50 visible wavelength photons per decay in media with index of refraction $n = 1.36$ to 1.4, such as biological tissue (Gill *et al* 2015). ^{82}Rb is the only common medical radionuclide which is brighter. Thus Cerenkov luminescence imaging can be a good option for imaging ^{90}Y, in particular in preclinical situations.

In the following, Cerenkov and PET imaging of ^{90}Y in a realistic small animal phantom was conducted using typical imaging parameters, and the results are quantified and compared.

2. Methods

2.1. Phantom

A commercially available plastic mouse phantom (XFM-2, PerkinElmer), with optical properties similar to tissue (Kuo *et al* 2007), was used for this experiment. Optical properties of the phantom range from $\mu_s' = 20$ cm^{-1} and $\mu_a = 0.4$ cm^{-1} at 580 nm to $\mu_s' = 10$ cm^{-1} and $\mu_a = 0.02$ cm^{-1} at 740 nm. The phantom has two holes which allow for placement of target inserts, and the locations of the holes are indicated on the CT scan images of the phantom shown in figure 1. The target inserts have in their narrow tip a small (5 μL) hollow which can be filled with solution, with the solution remaining in the insert tip through capillary action. Each insert was filled using a microliter syringe (Hamilton Company) with typically 4 μL of solution containing up to 150 μCi of ^{90}Y, and then at subsequent time points both CLI and PET imaging were performed with one or two of the inserts in place. Figure 2 shows the inserts with activity in the tips, as imaged separately in the optical imaging system. Comparing images with one and with two inserts in the phantom was a measure of both reproducibility and limitations due to non-local background. For CLI imaging, only the left insert, at 9 mm depth, was considered for analysis, and the presence or absence of the much deeper right insert provided two different background conditions. For PET and tomographic Cerenkov imaging, both target locations were used in analysis. Since a furless research mouse has typically a thickness of 22 mm or less, and can be placed in a dorsal, ventral, or side orientation, 9 mm is a depth unlikely to be exceeded in an imaging study of a single target.

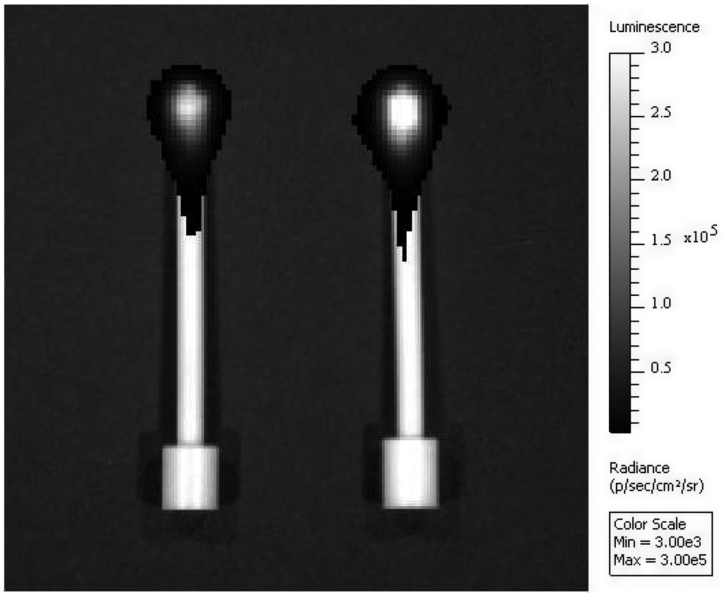

Figure 2. Inserts (of 50 mm length) with ^{90}Y activity, imaged in the optical system. The luminescence image (thresholded grey color scale) is overlaid on a photograph.

There was no radionuclide background in the phantom, which presents an ideal case of contrast in comparison to an *in vivo* experiment where significant non-specific activity may be present. For this phantom, the primary optical imaging background luminescence arose from afterglow of the phantom plastic material when it was exposed to white light; this was kept to a practical minimum by avoiding exposure to room lights and minimizing white light photographs of the phantom in the optical imaging system. For PET imaging, the dominant source of image background was the intrinsic activity of the ^{176}Lu present in the LSO scintillator detectors.

2.2. Imaging systems

Optical images were obtained with a commercial small animal imaging system (IVIS Spectrum, PerkinElmer) which has a sensitive CCD camera (Andor iKon, back-thinned and back-illuminated CCD cooled to −90 °C). PET images were obtained with a commercial small-animal PET scanner (Siemens Inveon DPET), whose performance has been thoroughly characterized (Bao *et al* 2009, Constantinescu and Mukherjee 2009, Visser *et al* 2009, Disselhorst *et al* 2010, Magota *et al* 2011).

2.3. Data sets

Several data sets were acquired for this study of ^{90}Y imaging: one for CLI detection limits; one for PET detection limits; and one for a comparison of tomographic Cerenkov and PET imaging. The ^{90}Y isotope was obtained as yttrium chloride in 0.5 M HCl (PerkinElmer Radiotherapeutics). Initial activity added to the inserts was measured in a dose calibrator and the estimated uncertainty is the greater of +/–5% (due to dependence on container and geometry from their influence on the generation of bremsstrahlung) or +/–0.5 μCi, as the dose calibrator does not have stable readout for very low activity levels. For each data set, images were then acquired over many hours and the time elapsed from the first image used to calculate the remaining activity in each insert.

2.3.1. Cerenkov detection limits

For Cerenkov detection limits, 4.5 μCi of ^{90}Y were added per insert. Over 625 h, 11 CLI data sets were acquired, approximately once every 50 to 70 h. At the final time point the activity in each of the inserts was less than 10 nCi. Each data set consisted of four image sequences, acquired with the phantom in a prone orientation, and with imaging system settings: *f/1*, large binning (120 by 120 pixel luminescence images), field of view C, and open filter. The sets consisted of the four sequences: (1) both inserts in the phantom, 10 images each of 30 s exposure; (2) both inserts in the phantom, 5 images each of 2 min exposure; (3) the upper (i.e. left) insert only in the phantom, 10 images each of 30 s exposure; and (4) the upper insert only in the phantom, 5 images each of 2 min exposure. The reason for repeating 10 times (for the shorter exposure time) or 5 times (longer exposure time) is to assess the statistical variations between images. Representative images with a 2 min exposure time are shown in figure 3.

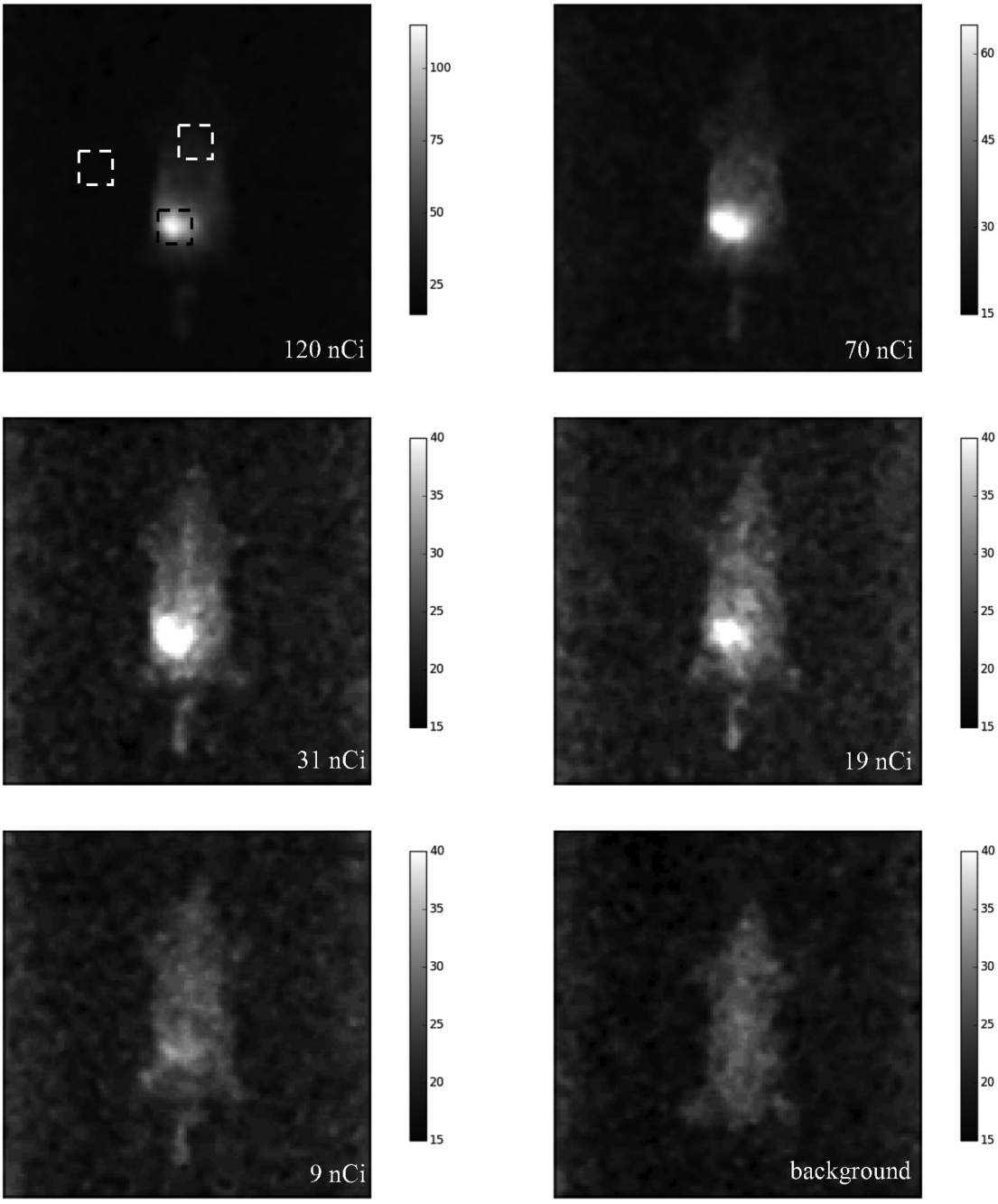

Figure 3. Sample single Cerenkov luminescence images from five timepoints, and an image of the phantom with no inserts. Each 120 × 120 pixel image is the raw luminescence image from a 2 min exposure, and has been background subtracted with a constant value (of 550 counts for all pixels), outlier pixels removed, and the image smoothed by a 3 × 3 pixel median filter. Three 10 × 10 pixel regions of interest (background, phantom background, target) are indicated on the first image. The colorscales represent counts per pixel and are thresholded at 15 counts. The activity per insert in the first five images (left to right, top to bottom) is 120, 70, 31, 19, and 9 nCi. The afterglow of the plastic material, even with minimized handling in room light, is apparent in the background image.

2.3.2. PET detection limits

For PET detection limits, 150 μCi of ^{90}Y were added per insert. Over 385 h, 6 PET data sets were acquired, with time elapsed between acquisitions of 40 to 100 h. At the final time point the activity in the inserts was 2.4 μCi per insert. Each data set consisted of two PET images, one with both inserts in the phantom and one with the upper insert only. The PET imaging consisted of 15 min acquisitions with standard settings of: energy window 350–650 keV, timing window 3.4 ns, span 3, ring difference 79. No attenuation or scatter corrections were used. Reconstruction was done by FBP into images of dimension 128 × 128 × 159, pixel size 0.776 × 0.776 × 0.796 mm^3, and images were processed with a 3D Gaussian filter (ImageJ, sigma = 2 pixels), resliced to a coronal orientation (as if the phantom were viewed from above) and a maximum intensity projection performed over the central 20 coronal slices (15.5 mm). Attempts to use OSEM or MAP

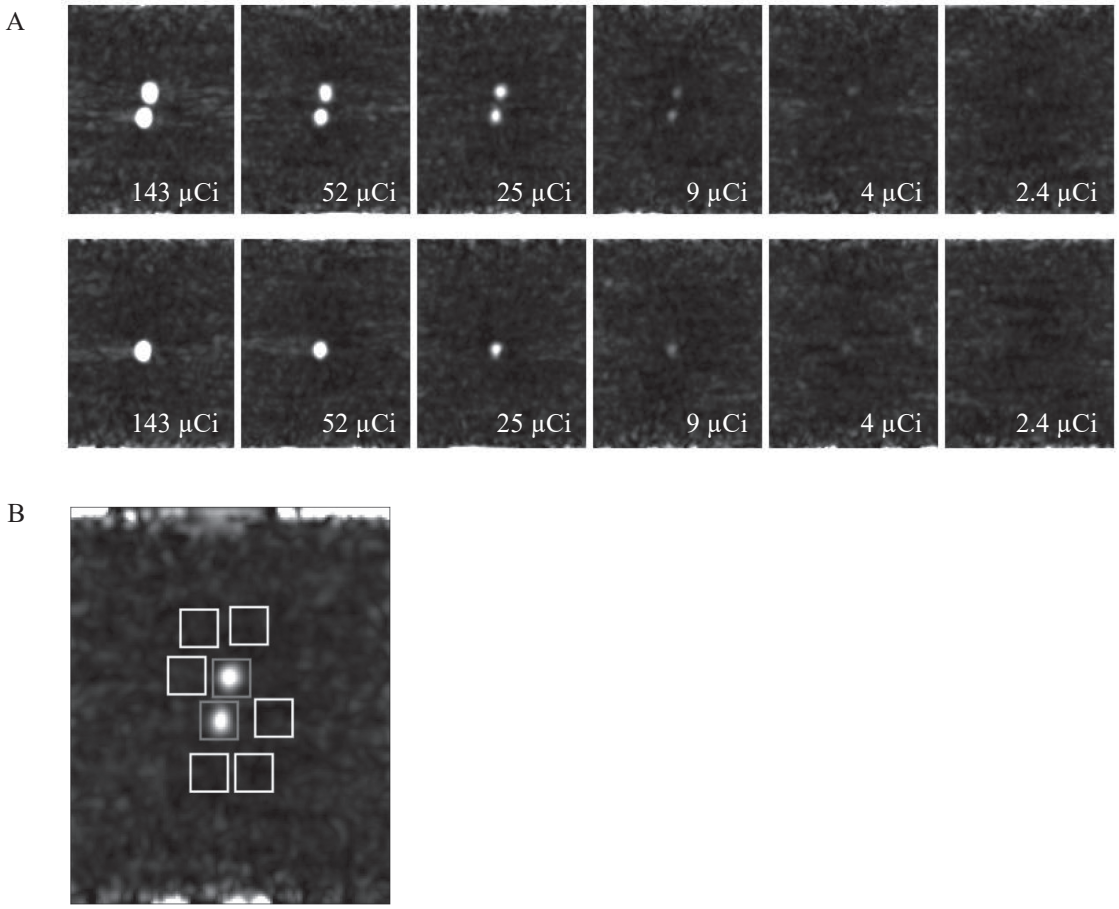

Figure 4. (A) PET image data. Images were acquired at six time points, shown left to right (activity in each insert at the time points: 143, 52, 25, 9, 4, 2.4 μCi). Each time point an image was acquired with one insert in the phantom and with two inserts in the phantom—hence the one and two bright spots in each upper/lower pair of images below. The PET images shown are obtained by Guassian smoothing the images in three dimensions with a sigma of 2 pixels, reslicing to a coronal orientation, and performing a maximum projection. All are shown with the same arbitrary colorscale, though the brightest image is saturated and the target spots have intensity 10x the max used for these images. (B) For each image two target ROIs were defined in the center and six ROIs defined in the outer portion of the image. Note that it appears the target spot regions converge to a point below the background value, an effect possibly caused by the plastic of the phantom reducing the LSO background coincidences.

reconstruction methods found little success in producing useful images, likely due to regularization smoothing away low number of counts. The resultant FBP-reconstructed PET images are shown in figure 4 with an arbitrary (i.e. uncalibrated) but not thresholded color scale. The images are the maximum intensity coronal projections, shown in pairs with first the two insert and then the one insert images given.

2.3.3. Cerenkov tomography and PET comparison

For tomographic Cerenkov (CLT) and PET imaging comparison, at four time points (0 hr, 70 hrs, 184 hrs, 287 hrs) the activity in each of the two targets was 150 μCi, 70 μCi, 21 μCi, and 7 μCi. PET imaging was a 30 min scan with acquisition settings and reconstruction parameters otherwise identical to those given above. CLT data consisted of sequences of filtered images, 30 s exposures at nine wavelengths from 580 nm to 740 nm (every 20 nm), in both dorsal and ventral orientations. In the dorsal orientation the closer target position is 9 mm below the surface, in the ventral orientation the closer target is 4 mm below that surface. In all Cerenkov images, the intensity is significantly dominated by the closer target position. The CLT reconstructions were done using the system software (LivingImage, version 4.4, PerkinElmer) algorithms (Kuo *et al* 2007) with the addition of a Cerenkov spectrum to the source spectra list. Best CLT results were obtained by: cropping the images and reconstructed 3D surface to exclude the head and limbs of the phantom; applying a threshold of 10% to all images; selection in the software of proper phantom material, orientation and optical properties; and most importantly, with selection of the specially added Cerenkov source spectrum (with a λ^{-2} wavelength dependence).

2.3.4. Images for comparison to in vivo applications

For comparison to actual applications, we considered some published studies using CLI with various isotopes: ^{90}Y (Aweda *et al* 2011, Lohrmann *et al* 2015), ^{90}Y and ^{177}Lu (Balkin *et al* 2014), ^{68}Ga (Fan *et al* 2015), and ^{89}Zr (Natarajan *et al* 2013). Background in these *in vivo* studies was limited by animal autoluminescence light (Troy *et al* 2004), but was usually more significantly arising from non-specific radiotracer biodistribution. Injected dose (i.d.) levels used for imaging shown in these published studies were: 8 μCi ^{90}Y (Aweda *et al* 2011); 20–500 μCi ^{90}Y (Lohrmann *et al* 2015); 100 μCi ^{90}Y and ^{177}Lu (Balkin *et al* 2014); 100 μCi ^{68}Ga (Fan *et al* 2015); and 100 μCi ^{89}Zr (Natarajan *et al* 2013). Note that for Cerenkov light output, ^{68}Ga has approximately 70% the light output of ^{90}Y per decay, ^{89}Zr has approximately 5% the output of ^{90}Y per decay, and ^{177}Lu has 0.5% the output of ^{90}Y per decay (Gill *et al* 2015).

For comparison to the phantom images of the current study, two of the images from figure 3 were considered: those corresponding to 70 nCi and 9 nCi activity per insert.

2.4. Imaging analysis and comparisons

For CLI image analysis the images were initially viewed with the system software (LivingImage) but all quantitative processing and analysis shown here was performed using the raw luminescence images and Python/matplotlib code (Hunter 2007). For PET image analysis ImageJ (Rasband 2016) was used on the reconstructed images.

Imaging comparison of PET versus CLI (with ^{90}Y) was necessarily based on several assumptions. PET is an inherently tomographic modality, and for small animal imaging PET is fairly uniform in sensitivity, spatial resolution, and quantitative contrast recovery over the entire field of view (Goertzen *et al* 2012). Optical imaging modalities, including CLI, are most often acquired as single images of the emitted light as observed from one view of the surface of the subject; this is true even if images are acquired at many wavelengths to permit a tomographic reconstruction or spectral unmixing. For optical imaging the sensitivity, resolution, and quantitative performance are much less robust and extremely nonuniform in comparison to PET. The most valuable and typical use for CLI in small animal imaging applications is in obtaining (semi)quantitative biodistribution of a radiolabeled probe, possibly in a xenograft tumor model. Applications requiring high-quality and truly quantitative tomographic images are most likely to be best approached with PET imaging with a high-yield PET radionuclide. For comparison of the modalities in ^{90}Y imaging we chose to evaluate PET images obtained with typical parameters and CLI images obtained using a feasible protocol with exposure times of 30 s or 120 s. Images were evaluated for both modalities by considering regions of interest (ROI) centered on the known target locations, and comparing the signal obtained there to the signal from an identically-sized ROI located elsewhere within or on the phantom.

Contrast to noise ratios (CNR) were used here as the primary figure of merit for an image (Rose 1948, Currie 1968, Bao and Chatziioannou 2010, Cherry *et al* 2012). For these data sets, there was infinite phantom contrast and so calculating a contrast recovery coefficient was not meaningful. As a definition of a detection limit, the Rose criterion was used: CNR > 4. ROIs for calculating signal and background, and thus contrast and noise, were chosen to be of a fixed and equal size (10 × 10 pixels for CLI optical images, 15 × 15 pixels for PET images; both roughly 1 × 1 cm^2), thus avoiding issues with considering individual image pixel characteristics and unknown feature size. Contrast was calculated from signal and background ROI values (averaged over multiple images if taken), and noise was calculated from a standard deviation of multiple background ROIs.

To establish quantification limits with CLI and PET, one definition is signal greater than or equal to ten times the image noise (Currie 1968); this is essentially equivalent to an activity of 2.5x the Rose criterion. An alternative measure, which was calculated here, is to consider the linearity of background subtracted ROI values with respect to known activity (as obtained from time decay). The ROI values versus activity were fit to a straight line ($y = kx$) with no offset, and the quantification limit identified as the point above which the data are within 5% of the linear fit. The 5% value is an arbitrary threshold based on the fit residuals shown in figure 6(C). This assumes that the imaging system was linear (no saturated CCD pixels, no random coincidence or dead time effects in PET) in its response at the larger activity values under fitting; for the activity levels considered here that is a comfortable assumption.

For CLI images, a 10 × 10 pixel signal ROI was chosen centered on the brightest area of the upper (left) insert location. Signal was defined as S = I–B, where I is the image intensity (sum of the pixel values) in the ROI, and B is a background ROI obtained from an identically-sized but different area of the image. The background ROI was chosen for the CLI data to be located on the phantom, on the region at the back of the neck as shown in figure 3. A second background ROI, the camera background B_C, was chosen in the image to the side of the phantom. Contrast in the images was defined by C = S/B.

Contrast to noise ratio for CLI images was calculated by first finding the noise value $\sigma = (\sigma_B^2 + \sigma_{BC}^2)^{(½)}$, obtained from adding in quadrature the standard deviations of the five or ten B ROI values to obtain σ_B, and

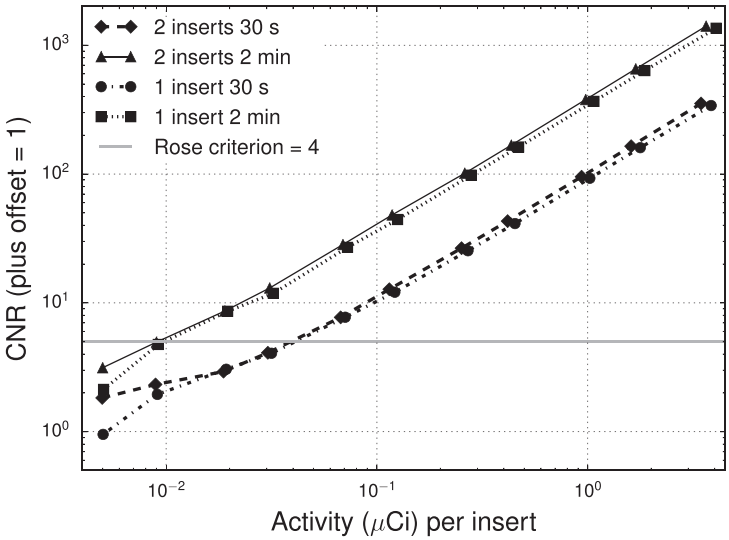

Figure 5. CLI image CNR results verus activity per insert. Note that the horizontal axis is oriented so that the time sequence of the data (decreasing activity) goes from right to left. A vertical offset (= 1) is added to the points to allow plotting on a log scale. The Rose criterion (CNR > 4) is shown and yields a detection limit for the 9 mm deep target location of 10 nCi for a 2 min CLI acquisition. For the shorter acquisition images the detection limit is 40 nCi. The very small differences between the 1 insert and 2 inserts curves show that the imaging is dominated by the upper insert, that the background contribution of the second deeper insert (if present) is small. For the 2 inserts data points only the upper insert location is analyzed.

of the B_C values to obtain σ_{BC}. This was done to account for the statistical variations in the difference of B-B_C, which is the background in the phantom minus the camera background. Then the final calculation was CNR = $C/(\sigma/B) = S/\sigma$. Note that the luminescence images have a constant offset (essentially the mean value of B_C) whose exact value was irrelevant in calculating S or σ_B, though in performing the actual calculations and in displaying the images in figure 3, a value of 550 counts was first subtracted from all image pixels. The σ_B and σ_{BC} values between data sets were reasonably similar (σ_B values varied from 80 to 200 counts, σ_{BC} varied from 50 to 60 counts; values were calculated from the sums of the pixels in the 100 pixel ROIs). For final calculations of CLI CNR, a single value (σ = 145 counts) was used, obtained from averaging σ over all data sets.

For PET image analysis, 15 × 15 pixel ROIs were used, as shown in figure 4(B): one or two ROIs for the insert target locations, and the six selected background ROI locations. For CLI imaging the noise factor was calculated from standard deviations of multiple repeated images, but for the PET imaging noise was calculated from standard deviations of multiple background ROIs on a single image. As with the CLI data, the noise values obtained from the PET background ROIs were quite close to each other and thus a single average value is used for all CNR calculations. CNR was calculated from each PET image by taking the image ROI values I_{PET} from the target locations, the mean value B_{PET} from the six background locations, and σ_{BPET} (the averaged standard deviations of the background values) as:
$CNR = ((I_{PET} - B_{PET})/B_{PET})/(\sigma_{BPET}/B_{PET}) = (I_{PET} - B_{PET})/\sigma_{BPET}$.

3. Results

3.1. CLI detection limits for ^{90}Y

The CNR results from analyzing the four types of images in this data set (1 or 2 inserts; 30 s or 120 s exposures) are given in figure 5, and show a negligible effect from the presence or absence of the 2nd insert on the CNR for the upper/left one. There is a significant difference between the CNR curves for the shorter and longer exposure times.

Applying the Rose criterion to the CNR (figure 6(B)) we found a detection limit for 2 min image exposures to be 10 nCi (37 Bq). This is consistent with visual inspection of the images (see figure 3) where there is a clear bright spot in the image with 19 nCi (middle right) but not so with the 9 nCi image (lower left). Similarly, from the CNR curve for 30 s image exposures, the detection limit is 40 nCi (148 Bq).

3.2. PET detection limits for ^{90}Y

For PET imaging, applying the Rose criterion to the CNR for the acquired images, from figure 7 the detection limit is between 6 μCi and 10 μCi per insert (from the one insert and two insert data sets in figure 7(B)). This is consistent with visual inspection of the images shown in figure 4, where the images with

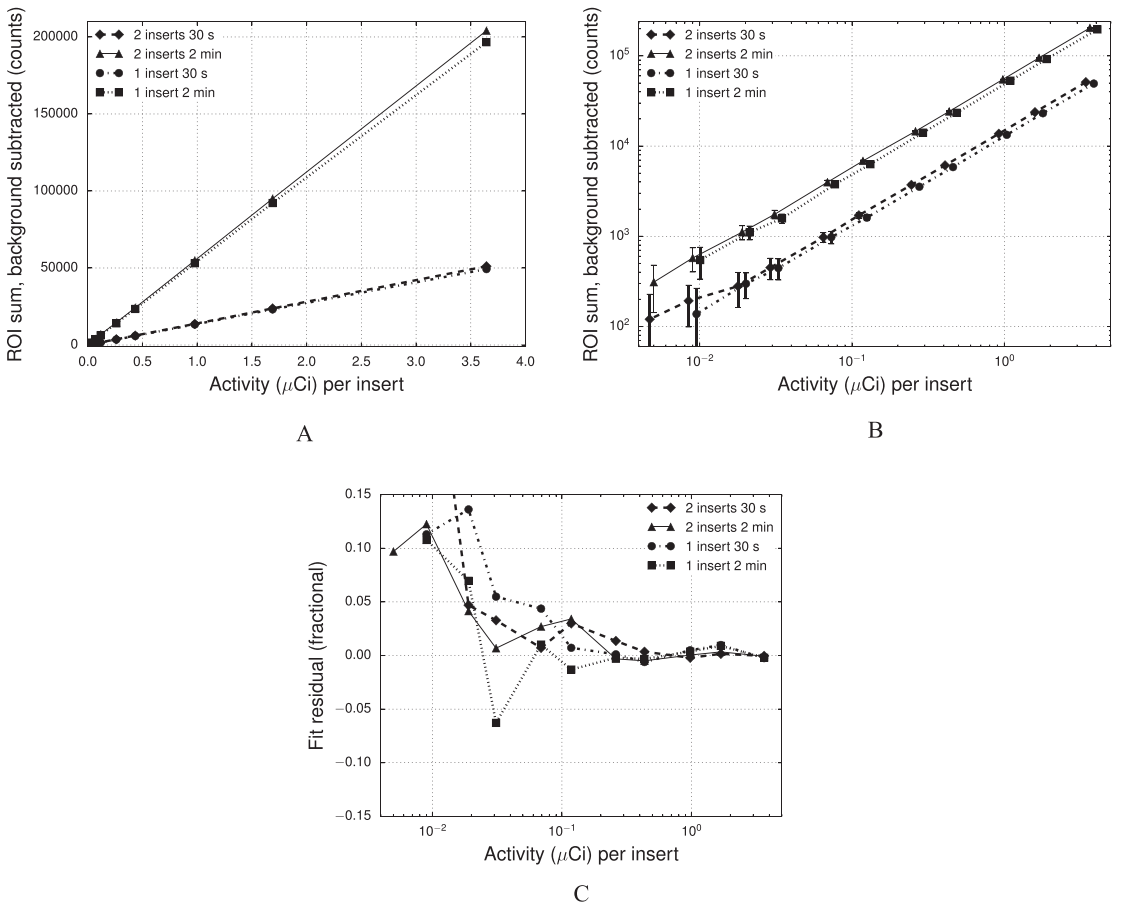

Figure 6. CLI background subtracted ROI values versus activity (A linear scale; B log-log scale, points slightly staggered for visibility), and residuals from a linear fit (C). The fits are not shown on the plots since they are indistinguishable from the data except for the lowest activity points. The fits are forced to go through the origin (i.e. fits are single parameter fits to lines of the form $y = kx$). For the quantitative imaging limit definition used here of linearity within a fractional difference of 0.05 (i.e. 5%), the result here is 0.1 μCi per insert.

9 μCi in each insert show up fairly clearly, but at 4 μCi they do not. For a detection limit result the value of 10 μCi is chosen as a round figure.

3.3. Quantification performance for CLI and PET

The linear nature of the CLI data, for background subtracted CCD image counts versus insert activity, is readily apparent from figure 6. From the CLI imaging, fitting results for the four data sets, the slopes of the lines were: 14.0 counts/nCi (30 s exposure image, 2 inserts); 56.1 counts/nCi (120 s exposure image, 2 inserts); 13.6 counts/nCi (30 s exposure image, 1 insert); and 54.1 counts/nCi (120 s exposure images, 1 insert). From figure 6(C), the fractional residuals for all of the data sets were within 0.05 (5%) for 70 nCi and above.

The agreement of the PET data with a linear fit was not as good over the activity levels considered in figure 7(C). The best fit line (shown as a curve on the semi-log plot) was only within 10% of the data for the two highest activity points, suggesting that quantitatively accurate ^{90}Y PET imaging requires larger than 25 μCi (the third highest point) in a cm-scale ROI.

3.4. CLT results and comparison to PET imaging

Figure 8 displays the result of CLT reconstruction on the first timepoint of the data set (both inserts with 150 μCi ^{90}Y). For all four time points (smallest activity per insert value of 7 μCi), in both dorsal and ventral orientations, the two sources were able to be reconstructed as separate sources with centers within 2 mm of the true locations, which can be considered quite successful results. For each of the four timepoints there were the two sources and the two orientations, giving four quantitative results; these are plotted versus the nominal activity in figure 9 and are again in good agreement with each other, remarkably so given the range in depths from 4 to 18 mm. The average PET ROI result (averaged over the two inserts) is shown at each time point as well.

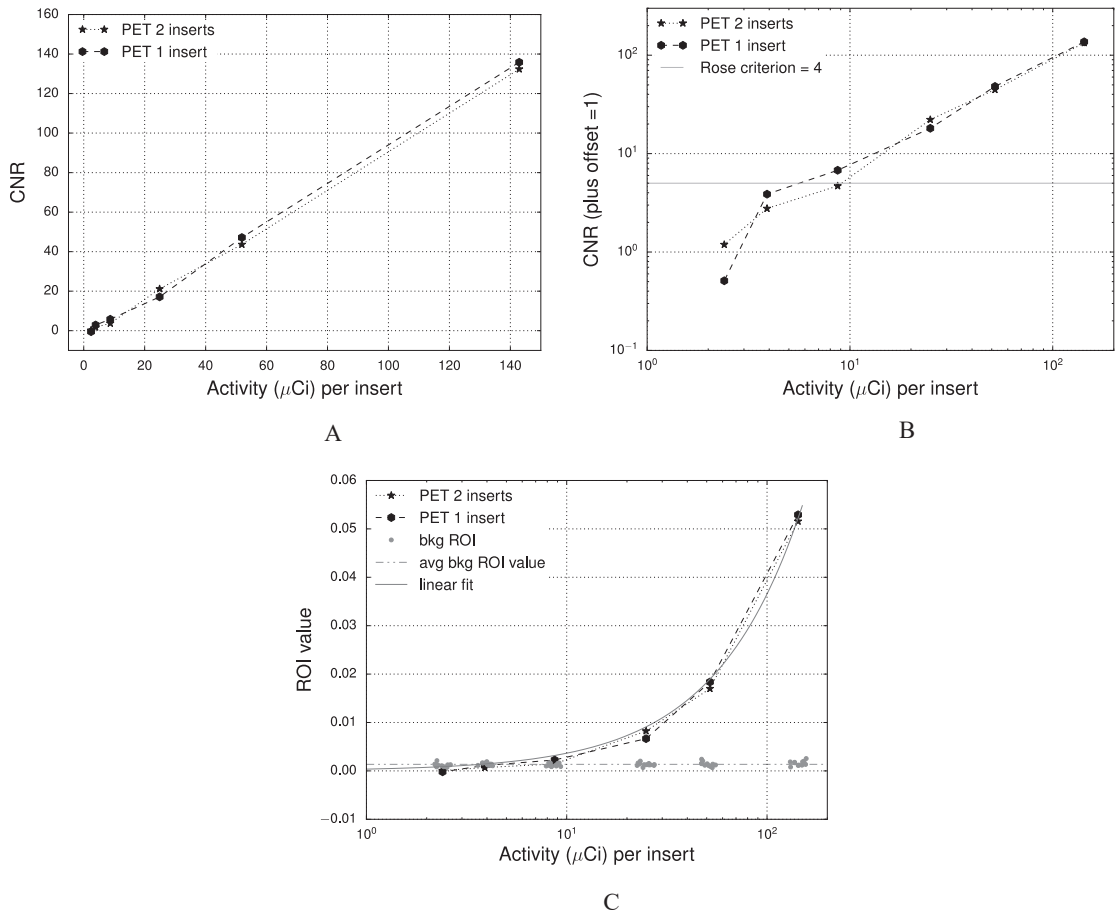

Figure 7. (A and B) PET image CNR results versus activity per insert. The two subfigures A and B show the same data points but with linear and log scales. The 2 inserts points are the average of the two ROIs for those images. Note that the horizontal axes are oriented with increasing activity so that the time sequence of the data sets as acquired goes from right to left. A constant offset (equal to 1) has been added to the y coordinates of the data points for the log-log plot to make the values all positive for plotting purposes. (C) Background subtracted ROI values (y-axis scale is arbitrary units) for the two insert images (average of the two ROIs), and for the one insert images. The background values (slightly scattered for visibility) and the overall average background value are shown for each time point. The linear fit (forced to go through the origin) is only within 10% of the data for the two highest activity points.

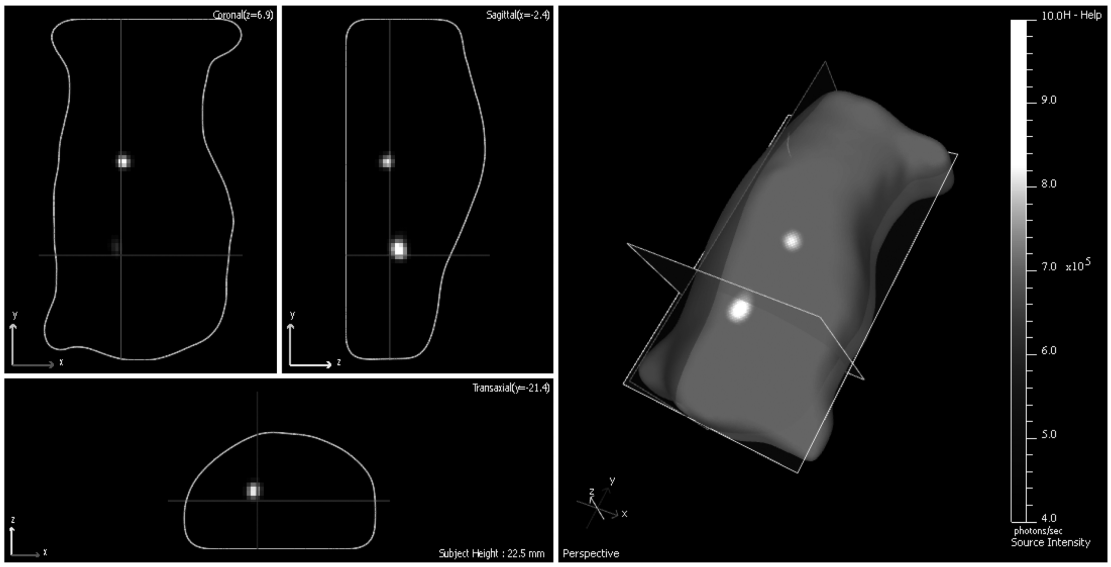

Figure 8. Sample display of tomographic reconstruction result from CLT data set. In this background-free case in a homogenous medium, the imaging is successful as the two insert targets are clearly reconstructed and resolved as individual sources. This shows the reconstruction from the first time point acquired, where the inserts each had 150 μCi ^{90}Y.

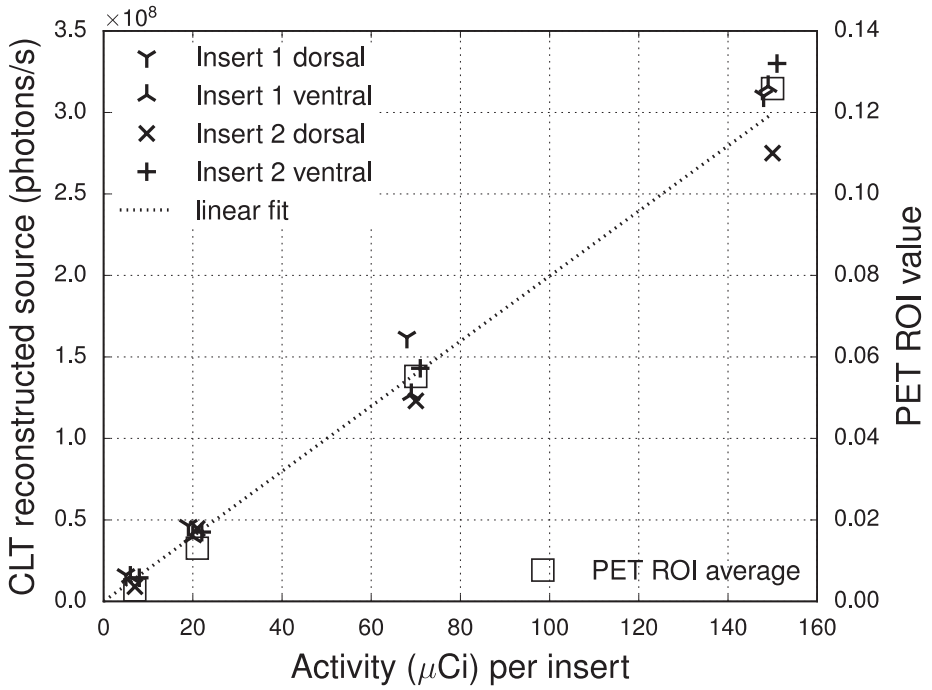

Figure 9. At four timepoints, multi-wavelength data sets were obtained of the phantom with both inserts (in each of dorsal and ventral orientation, a total of eight data sets). For the eight CLT reconstructions of the phantom containing two inserts (a total of 16 three-dimensional ROI results), the reconstructed source intensity is plotted versus the nominal activity of each insert. A straight line fit ($y = kx$) for the CLT data is also shown. PET average (over the two inserts, scale is arbitrary units) three-dimensional ROI values are also plotted for each time point, with an independent scale for the y-axis on the right.

3.5. Comparison to in vivo images

To set a comparison to *in vivo* images, the two selected phantom images from figure 3 were both analyzed using the quantitative settings on the system software, and both had a background radiance from the phantom (ROI on the phantom neck area) of 300 p/s/cm^2/sr. The 70 nCi activity per insert image had a peak radiance in the insert target ROI of 1700 p/s/cm^2/sr, and the 9 nCi image had a peak radiance value of 440 p/s/cm^2/sr. These images correspond to the identified limits for detection (9 nCi) and quantification (70 nCi) for a 120 s exposure.

From the listed references, typical radiance values of the animal in areas other than specific uptake locations (inferred from thresholds on images if not otherwise visible) range from lower values such as 200 p/s/cm^2/sr (Aweda *et al* 2011) and 500 p/s/cm^2/sr (Lohrmann *et al* 2015) (images acquired 24 h or greater post injection, allowing probe clearance), to higher values of 2000 p/s/cm^2/sr [Natarajan *et al* 2013], 3000 p/s/cm^2/sr [Fan *et al* 2015], and 7×10^4 p/s/cm^2/sr (100 μCi ^{90}Y images in [Balkin *et al* 2014]). Thus the background levels of the plastic phantom are of a similar scale to those found in studies using low activity levels of ^{90}Y (20 μCi or less i.d. per animal), or using isotopes which are not as bright. These references all found at least semiquantitative use of their CLI images, and in some cases excellent agreement with *ex vivo* biodistribution data, and had contrast ranging from 2:1 to 10:1 for the brightest area on the animal surface compared to the rest of the animal.

4. Discussion and conclusions

There are obvious limitations of the measurements presented here of a phantom, in comparison to real *in vivo* applications: the ^{90}Y sources were at constant locations, and were highly localized; there was no non-specific radionuclide background; there was no structure to the background in images; and due to the homogenous nature of the phantom, light reaching the surface of the phantom had been transported in a relatively simple manner. However, these limitations largely serve to control for these many potentially confounding variables and isolate the dependence of image intensity versus activity for a source area in the image. The comparisons to CLI images in the literature show that the background values with the phantom were not inconsistent with a reasonable low-activity *in vivo* imaging situation.

For the CLT study, the tomography results obtained are encouraging, though this is helped by fairly high activity levels and the factors mentioned above (no background sources and a homogenous phantom). However, experience with *in vivo* studies suggests that CLT is at the moment too sensitive to the algorithm

and method (which wavelengths, surface profile, masking and thresholding); the successful results here were arrived at somewhat by tuning the algorithm to achieve a known result. Attempts to use CLT algorithms to achieve better quantification or to detect or resolve deeper sources *in vivo* are not likely to be robust enough to perform better than simple planar imaging for most cases.

To summarize the results of this work with ^{90}Y imaging in small animal applications, in cases of very low background and localized sources, at source depths of up to 9 mm, CLI can be successful for detecting activity down to 10 nCi, and PET with a LSO detector-based scanner can be used for detecting activity as low as 6 μCi. For quantitative (or at least semiquantitative) imaging CLI can be effective for targets of 70 nCi or greater; PET can be effective for targets of 25 μCi or greater. CLI limits could be pushed lower with longer image acquisition times but as seen in the *in vivo* comparisons, in any practical application the animal background will limit performance. CLT methods may continue to develop but successes with reconstructions of targets of 7 μCi of ^{90}Y or greater in a homogenous plastic phantom are not yet indicative of utility in an *in vivo* setting.

There are not likely many or any cases where CLT imaging will prove superior to PET imaging; rather the primary conclusion of this study is that for imaging of ^{90}Y, CLI imaging can potentially outperform PET for preclinical imaging for qualitative biodistribution studies. As ^{90}Y is seeing increased use for clinical therapy applications, the isotope is of translational interest. ^{90}Y is the best (brightest) useful Cerenkov isotope, so even independent of PET imaging, quantifying limits for preclinical studies is of interest.

These limits on PET and CLI imaging of ^{90}Y will vary for an *in vivo* case for different depths of the region of interest, and for varying contrast of the signal to the *in vivo* background, especially in the case of a nonuniform background. Activity levels above these limits should be visible on imaging, and for CLI should allow at least semiquantitative imaging for uptake reasonably near the surface (xenograft tumors, kidneys, spleen, and possibly liver). The results presented here can guide experimental design for necessary injected dose (i.d.) values for small animal ^{90}Y imaging studies—for example: with a 10 μCi i.d., a 2% i.d./g uptake, and a tissue volume of mass 0.5 g, the result is 100 nCi in the target area, which should be easily detected for depths of up to several mm.

Acknowledgments

The authors would like to thank Chaincy Kuo and Julie Czupryna of PerkinElmer, Inc. for assistance with CLT reconstructions. Additionally the authors would like to thank Justin Klein and Emilie Roncali of UC Davis for helpful discussions. Research reported in this publication was supported by the Institute of Biomedical Imaging and Bioengineering of the National Institutes of Health under Award Number R01 EB015471.

ORCID iDs

Gregory S Mitchell https://orcid.org/0000-0002-8276-1107
P N Thomas Lloyd https://orcid.org/0000-0002-4271-8809
Simon R Cherry https://orcid.org/0000-0002-0155-5644

References

Attarwala A A, Molina-Duran F, Büsing K-A, Schönberg S O, Bailey D L, Willowson K and Glatting G 2014 Quantitative and qualitative assessment of Yttrium-90 PET/CT imaging *PLoS One* **9** e110401

Aweda T A, Eskandari V, Kukis D L, Boucher D L, Marquez B V, Beck H E, Mitchell G S, Cherry S R and Meares C F 2011 New covalent capture probes for imaging and therapy, based on a combination of binding affinity and disulfide bond formation *Bioconjugate Chem.* **22** 1479–83

Balkin E R *et al* 2014 In vivo localization of ^{90}Y and ^{177}Lu radioimmunoconjugates using Cerenkov luminescence imaging in a disseminated murine leukemia model *Cancer Res.* **74** 5846–54

Bao Q and Chatziioannou A F 2010 Minimum detectable activity estimation for preclinical PET *Med. Phys.* **37** 6070–83

Bao Q, Newport D, Chen M, Stout D B and Chatziioannou A F 2009 Performance evaluation of the Inveon dedicated PET preclinical tomograph based on the NEMA NU-4 standards *J. Nucl. Med.* **50** 401–8

Barber T W, Yap K S, Cherk M H, Powell A and Kalff V 2013 Comparison of positron emission tomography/CT and bremsstrahlung imaging following Y-90 radiation synovectomy *J. Med. Imaging Radiat. Oncol.* **57** 567–71

Cherry S R, Sorenson J A and Phelps M E 2012 *Physics in Nuclear Medicine* 4th edn (Philadelphia, PA: Saunders)

Chi C, Du Y, Ye J, Kou D, Qiu J, Wang J, Tian J and Chen X 2014 Intraoperative imaging-guided cancer surgery: from current fluorescence molecular imaging methods to future multi-modality imaging technology *Theranostics* **4** 1072–84

Ciarrocchi E and Belcari N 2017 Cerenkov luminescence imaging: physics principles and potential applications in biomedical sciences *EJNMMI Phys.* **4** 14

Constantinescu C C and Mukherjee J 2009 Performance evaluation of an Inveon PET preclinical scanner *Phys. Med. Biol.* **54** 2885

Currie L A 1968 Limits for qualitative detection and quantitative determination *Anal. Chem.* **40** 586–93

D'Arienzo M 2013 Emission of β+ particles via internal pair production in the 0+ – 0+ transition of ^{90}Zr: historical background and current applications in nuclear medicine imaging *Atoms* **1** 2–12
De León-Rodríguez L M and Kovacs Z 2008 The synthesis and chelation chemistry of DOTA—peptide conjugates *Bioconjugate Chem.* **19** 391–402
Disselhorst J A, Brom M, Laverman P, Slump C H, Boerman O C, Oyen W J, Gotthardt M and Visser E P 2010 Image-quality assessment for several positron emitters using the NEMA NU 4-2008 standards in the Siemens Inveon small-animal PET scanner *J. Nucl. Med.* **51** 610–17
Elschot M, Vermolen B J, Lam M G, de Keizer B, van den Bosch M A and de Jong H W 2013 Quantitative comparison of PET and Bremsstrahlung SPECT for imaging the in vivo yttrium-90 microsphere distribution after liver radioembolization *PLoS One* 8 e55742
Fan D *et al* 2015 ^{68}Ga-labeled 3PRGD$_2$ for dual PET and Cerenkov luminescence imaging of orthotopic human glioblastoma *Bioconjugate Chem.* **26** 1054–60
Gill R K, Mitchell G S and Cherry S R 2015 Computed Cerenkov luminescence yields for radionuclides used in biology and medicine *Phys. Med. Biol.* **60** 4263–80
Goertzen A L *et al* 2012 NEMA NU 4-2008 comparison of preclinical PET imaging systems *J. Nucl. Med.* **53** 1300–9
Grootendorst M R, Cariati M, Kothari A, Tuch D S and Purushotham A 2016 Cerenkov luminescence imaging (CLI) for image-guided cancer surgery *Clin. Transl. Imaging* **4** 353–66
Hu H *et al* 2015 Feasibility study of novel endoscopic Cerenkov luminescence imaging system in detecting and quantifying gastrointestinal disease: first human results *Eur. Radiol.* **25** 1814–22
Hunter J D 2007 Matplotlib: a 2D graphics environment *Comput. Sci. Eng.* **9** 90–95
Kukis D L, DeNardo S J, DeNardo G L, O'Donnell R T and Meares C F 1998 Optimized conditions for chelation of yttrium-90-DOTA immunoconjugates *J. Nucl. Med.* **39** 2105–10
Kuo C, Coquoz O, Troy T L, Xu H and Rice B W 2007 Three-dimensional reconstruction of in vivo bioluminescent sources based on multispectral imaging *J. Biomed. Opt.* **12** 024007
Larson S M, Carrasquillo J A, Cheung N K V and Press O W 2015 Radioimmunotherapy of human tumours *Nat. Rev. Cancer* **15** 347–60
Liu H, Carpenter C M, Jiang H, Pratx G, Sun C, Buchin M P, Gambhir S S, Xing L and Cheng Z 2012 Intraoperative imaging of tumors using Cerenkov luminescence endoscopy: a feasibility experimental study *J. Nucl. Med.* **53** 1579–84
Lohrmann C, Zhang H, Thorek D L, Desai P, Zanzonico P B, O'Donoghue J, Irwin C P, Reiner T, Grimm J and Weber W A 2015 Cerenkov luminescence imaging for radiation dose calculation of a ^{90}Y-labeled gastrin-releasing peptide receptor antagonist *J. Nucl. Med.* **56** 805–11
Lubberink M and Herzog H 2011 Quantitative imaging of ^{124}I and ^{86}Y with PET *Eur. J. Nucl. Med. Mol. Imag.* **38** S10–S18
Magota K, Kubo N, Kuge Y, Nishijima K, Zhao S and Tamaki N 2011 Performance characterization of the Inveon preclinical small-animal PET/SPECT/CT system for multimodality imaging *Eur. J. Nucl. Med. Mol. Imag.* **38** 742–52
Maughan N M *et al* 2018 Multi institutional quantitative phantom study of yttrium-90 PET in PET/MRI: the MR-QUEST study *EJNMMI Phys.* **5** 7
Minarik D, Sjögreen Gleisner K and Ljungberg M 2008 Evaluation of quantitative ^{90}Y SPECT based on experimental phantom studies *Phys. Med. Biol.* **53** 5689–703
Mitchell G S, Gill R K, Boucher D L, Li C and Cherry S R 2011 In vivo Cerenkov luminescence imaging: a new tool for molecular imaging *Phil. Trans. R. Soc. A* **369** 4605–19
Natarajan A, Habte F, Liu H, Sathirachinda A, Hu X, Cheng Z, Nagamine C M and Gambhir S S 2013 Evaluation of ^{89}Zr-rituximab tracer by Cerenkov luminescence imaging and correlation with PET in a humanized transgenic mouse model to image NHL *Mol. Imaging Biol.* **15** 468–75
Nayak T K and Brechbiel M W 2011 ^{86}Y based PET radiopharmaceuticals: radiochemistry and biological applications *Med. Chem.* **7** 380–8
Nickles R J, Roberts A D, Nye J A, Converse A K, Barnhart T E, Avila-Rodriguez M A, Sundaresan R, Dick D W, Hammas R J and Thomadsen B R 2004 Assaying and PET imaging of Yttrium-90: 1»34 ppm>0 *2004 IEEE Nucl. Sci. Symp. Conf. Rec.* **6** 3412–14
Padia S A, Alessio A, Kwan S W, Lewis D H, Vaidya S and Minoshima S 2013 Comparison of positron emission tomography and bremsstrahlung imaging to detect particle distribution in patients undergoing Yttrium-90 radioembolization for large hepatocellular carcinomas or associated portal vein thrombosis *J. Vasc. Interventional Radiol.* **24** 1147–53
Pasciak A S, Bourgeois A C, McKinney J M, Chang T T, Osborne D R, Acuff S N and Bradley Y C 2014 Radioembolization and the dynamic role of ^{90}Y PET/CT *Front. Oncol.* **4** 38
Rasband W S 1997–2016 *ImageJ* (Bethesda, MD: U. S. National Institutes of Health) http://imagej.nih.gov/ij/
Robertson R, Germanos M S, Manfredi M G, Smith P G and Silva M D 2011 Multimodal imaging with ^{18}F-FDG PET and Cerenkov luminescence imaging after MLN4924 treatment in a human lymphoma xenograft model *J. Nucl. Med.* **52** 1764–9
Rose A 1948 The sensitivity performance of the human eye on an absolute scale *J. Opt. Soc. Amer.* **38** 196–208
Ruggiero A, Holland J P, Lewis J S and Grimm J 2010 Cerenkov luminescence imaging of medical isotopes *J. Nucl. Med.* **51** 1123–30
Scott N P and McGowan D R 2019 Optimising quantitative ^{90}Y PET imaging: an investigation into the effects of scan length and Bayesian penalised likelihood reconstruction *EJNMMI Res.* **9** 40
Selwyn R G, Nickles R J, Thomadsen B R, DeWerd L A and Micka J A 2007 A new internal pair production branching ratio of ^{90}Y: The development of a non-destructive assay for ^{90}Y and ^{90}Sr *Appl. Radiat. Isot.* **65** 318–27
Takahashi A, Himuro K, Yamashita Y, Komiya I, Baba S and Sasaki M 2015 Monte Carlo simulation of PET and SPECT imaging of ^{90}Y *Med. Phys.* **42** 1926–35
Troy T, Jekic-McMullen D, Sambucetti L and Rice B 2004 Quantitative comparison of the sensitivity of detection of fluorescent and bioluminescent reporters in animal models *Mol. Imag.* **3** 9–23
van Leeuwen F W B, Hardwick J C H and van Erkel A R 2015 Luminescence-based imaging approaches in the field of interventional molecular imaging *Radiology* **276** 12–29
Visser E P, Disselhorst J A, Brom M, Laverman P, Gotthardt M, Oyen W J and Boerman O C 2009 Spatial resolution and sensitivity of the Inveon small-animal PET scanner *J. Nucl. Med.* **50** 139–47
Willowson K P, Tapner M, QUEST Investigator Team and Bailey D L 2015 A multicentre comparison of quantitative (90)Y PET/CT for dosimetric purposes after radioembolization with resin microspheres: the QUEST phantom study *Eur. J. Nucl. Med. Mol. Imag.* **42** 1202–22

Wright C L, Zhang J, Tweedle M F, Knopp M V and Hall N C 2015 Theranostic imaging of Yttrium-90 *Biomed. Res. Int.* **2015** 481279
Xu Y, Chang E, Liu H, Jiang H, Gambhir S S and Cheng Z 2012 Proof-of-concept study of monitoring cancer drug therapy with Cerenkov luminescence imaging *J. Nucl. Med.* **53** 312–7
Yoo J, Tang L, Perkins T A, Rowland D J, Laforest R, Lewis J S and Welch M J 2005 Preparation of high specific activity ^{86}Y using a small biomedical cyclotron *Nucl. Med. Biol.* **32** 891–7